Probabilistic Space Weather Modeling and its Impact on Space Situational Awareness and Space Traffic Management

Smriti Nandan Paul, Piyush M. Mehta
West Virginia University
Thomas Kelecy, Ryan Coder
The Aerospace Corporation

ABSTRACT

The uncertainty in a Low Earth Orbit (LEO) space object's future position is influenced by uncertainty in thermospheric density, which can vary significantly during active space weather conditions, e.g. geomagnetic storms. The exponential increase in the number of objects in LEO, and subsequent challenges to Space Traffic Management (STM), motivate this study of novel probabilistic density models, HASDM-ML and MSIS-UQ, and their potential for more realistic satellite state uncertainty quantification. Several "near-miss" use cases are examined for both "quiet" and "storm" atmospheric models at orbital altitudes representative of SpaceX's Starlink and Planet's Dove constellations. The impact of these novel density models is examined using metrics such as time of closest approach and probability of collision, and suggestions for future work necessary to complete an assessment of these models are discussed.

1. INTRODUCTION

According to the European Space Agency's (ESA's) 2023 *Annual Space Environment Report* [1], close to 2400 payloads with perigee altitudes ranging from 200 to 1750 km were launched in the year 2022. Except for a few hundred, all these payloads are from commercial operators. The record number of launches in 2022 continues the recent trend, which saw approximately 1200 and 1700 launches in 2020 and 2021, respectively, in the same orbital region. The increase in launch traffic and the number of resident space objects (RSOs) is expected to continue unabated and clutter the near-Earth space environment. There is a growing consensus among the advocates of space safety and space stakeholders that the following improvements are needed: first, better models and observational data to estimate the current and future location of space objects and second, better operational frameworks focusing on conjunction assessment and collision avoidance between tracked space objects [2, 3].

This work focuses on improvements in the characterization of uncertainty in the predicted states of space objects in the moderate/high-drag low Earth orbit (LEO) region with perigee altitudes below 1000 km. Reliable and consistent uncertainty characterization affects important Space Situational Awareness (SSA) / Space Traffic Management (STM) tasks such as conjunction assessment, collision avoidance, sensor tasking, tracking and custody, maneuver/anomaly detection, and re-entry predictions. More specifically, the analyses underscore the importance of atmospheric density uncertainty, which is a principal source of error in modeling drag perturbation force. Atmospheric drag is the largest source of dynamical uncertainty in the highly congested LEO region [4], and accurate estimates of the neutral atmospheric density can improve the confidence in satellite state estimates. The atmospheric composition and the neutral atmospheric density are functions of space weather conditions. Currently, there is an inadequate understanding of the various physical processes driving the neutral density variations in the ionosphere-thermosphere region. Empirical atmospheric density models, which are used in the current work, exploit the correlation between density values and geomagnetic/solar drivers such as F_{10}, S_{10}, a_p, K_p, and others. These drivers are only approximate indicators and are difficult to forecast. Coarse sampling of driver inputs and dependency on the orbits of calibration satellites can also induce errors in empirical models. Density modeling errors resulting from limited understanding can be particularly significant during active space weather conditions such as geomagnetic storms [5]. This paper aims to demonstrate improvements in LEO state uncertainty prediction and the impact of space weather uncertainty in probability of collision (Pc) computation using data-based probabilistic atmospheric density models.

Over the years, several physics-based and empirical density models have been proposed for the ionosphere-thermosphere system. Interested readers may refer to [6], which provides a hierarchy of model development for many well-known atmospheric density models. The high-fidelity physics-based models, which rely on solving the Navier–Stokes equations for the upper atmosphere, are computationally expensive and will not be addressed in this work. Empirical models are typically less accurate than physics-based models but better suited for computational efficiency lending themselves to operational use. In the recent past, several 'traditional' empirical models have seen great prediction improvements because of near real-time data incorporation from a large number of calibration satellites using techniques such as the Dynamic Calibration Atmosphere (DCA) algorithm [4]. Empirical density models can also be created from surrogate techniques using accelerometer data onboard the recent geodetic satellite missions such as the Challenging Minisatellite Payload (CHAMP) [7], the Gravity Recovery and Climate Experiment (GRACE) [8] and its Follow-on (GRACE-FO) mission [9], the Gravity Field and Steady-State Ocean Circulation Explorer (GOCE) [10], and the Swarm A/B/C satellites [11]. However, most of the existing neutral density models (empirical or otherwise) offer no estimate of the uncertainty associated with the predicted density, i.e., they are deterministic. Current operations ignore the atmospheric density uncertainty or make simplified assumptions when accounting for it, or they lump together many of the unmodeled errors into the uncertainties. A common practice to handle unmodeled errors in uncertainties involves adjusting the state covariance matrix by a scaling factor determined by the observed variances around the estimated trajectory [12, 13].

Each approach to density modeling has its advantages and disadvantages and this work demonstrates how discrepancies in the predicted uncertainties can occur when different models are used, for example, by different space operators. In addition, the degradation of the models during active solar events also affects the propagation errors depending on where solar events occur in the prediction timeline. Hence, the main goal of this work is to demonstrate the impacts of using different density models under both active and quiet solar conditions, and how the errors affect the 'realism' of propagated covariances and probabilities of collision. Section 2 presents a 'motivating example' that illustrates the consequences of erroneous predicted covariances in the probability of collision computations. A detailed description of the methodology used in this work begins by introducing the concept of probabilistic density modeling in section 3, error propagation for spatio-temporal correlation preservation in section 4, and probability of collision computations based on the Brute Force Monte Carlo and Foster's approaches presented in section 5. Analysis for two representative LEO satellites experiencing a conjunction under differing space weather conditions is presented in section 6. Section 7 concludes by summarizing how the results can improve space operations, and identifies additional work that will further verify these results and support future operational implementation.

2. MOTIVATING EXAMPLE

A motivating example is presented to help frame the motivation for this work. Two LEO satellites are in intersecting orbits as depicted in Fig. 1 where Satellite-1, illustrated in green, is in a 98° inclined orbit and Satellite-2 has a 43° inclined orbit. Table 1 shows the initial position and velocity states along with the area-to-mass ratios, which is used for atmospheric drag and solar radiation pressure. A 12x12 EGM96 Earth gravity, Sun and moon third-body perturbations, solar radiation pressure (SRP), and atmospheric drag models are used to propagate each satellite state out to 2-days where a 2 km close approach conjunction occurs at the end of the 2-day span. The separation distance and conjunction are shown in Fig. 2.

Table 1: Satellite-1 and Satellite-2 initial states

State Element	Satellite-1 Initial State	Satellite-2 Initial State
Pos-x (km)	-5009.26702514916	-782.479775661389
Pos-y (km)	628.9683714532	1633.61994422041
Pos-z (km)	-4676.11817494502	-6642.5595230199
Vel-x (km/s)	-1.35121618410399	6.31681873941101
Vel-y (km/s)	-7.47478393849756	-3.87411612296017
Vel-z (km/s)	0.443195271216529	-1.68735304061458
A/m (m^2/kg)	0.04	0.03

For this example, initial state errors are sampled from the initial covariances, i.e. representation of orbit determination results that would be used to initialize propagation, shown in Table 2 and added to the initial states in Table 1. The

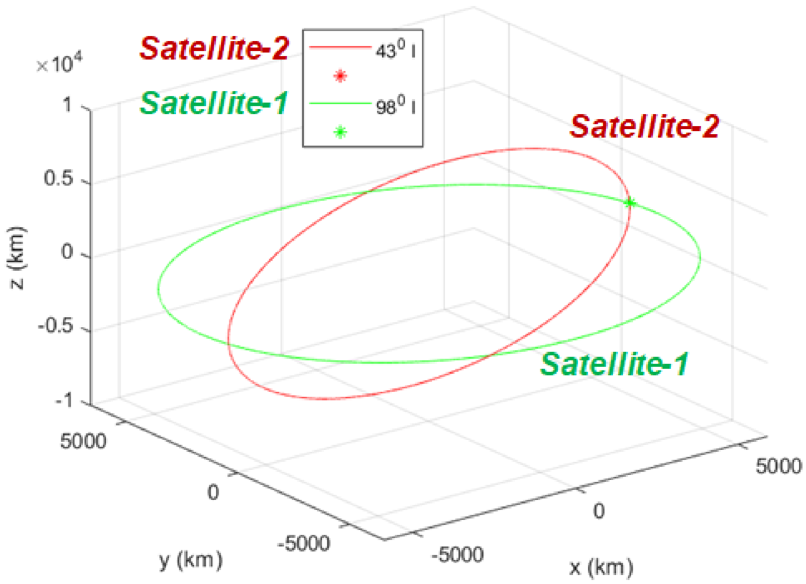

Fig. 1: Motivating example: two LEO satellite conjunction

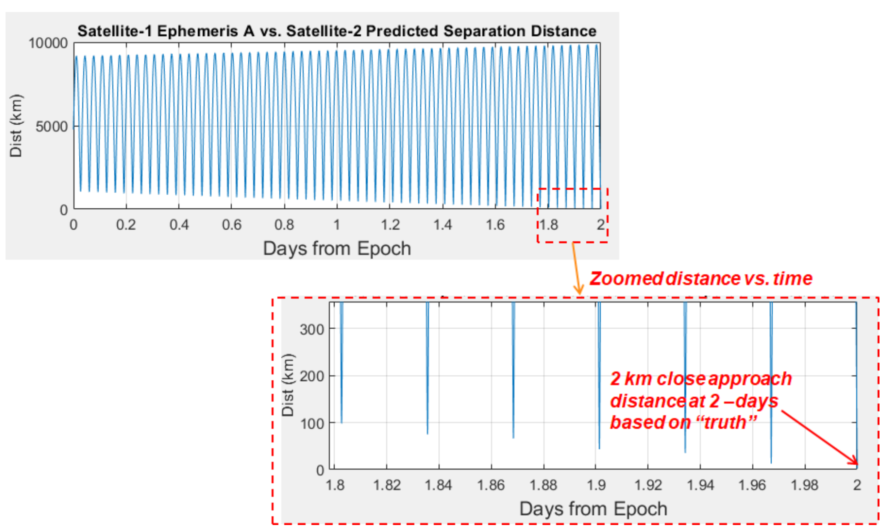

Fig. 2: Satellite-1 vs. Satellite-2 separation distance

mean state and covariance for each are propagated over two days using Unscented transforms, and the propagated covariances are compared to the propagation errors which are computed as differences relative to the propagated "truth" state, i.e. no initial state errors. Fig. 3 shows the propagation errors for Satellite-1 ephemerides A, left, and B, right, where the "nominal" initial covariances are used. The propagation errors, depicted with a blue line, which are computed as the differences between the "nominal" prediction and the known "truth" ephemeris, fall within the 3-σ error bounds, shown as red lines, of the propagated covariance as one would expect for cases where the errors are consistent with the covariance. However, when initial state errors for ephemeris B are sampled from the (larger) nominal, but the covariance is propagated using the (smaller) optimistic covariance (i.e. the covariance is unrealistic), one can see in Fig. 4 that the errors (blue line) now exceed the 3-σ covariance (red lines) bounds. It should be noted that, without knowledge of the "truth" state, one cannot determine with this information alone which covariance is inconsistent.

Table 2: Satellite-1 and Satellite-2 initial covariances

Initial State Covariance Element	Satellite-1 Covariance A Nominal	Satellite-1 Covariance B Nominal	Satellite-1 Covariance B Optimistic	Satellite-2 Covariance Nominal
Pos-x 1-sigma (m)	5.0	10.0	1.0	15.0
Pos-y 1-sigma (m)	5.0	10.0	1.0	15.0
Pos-z 1-sigma (m)	5.0	10.0	1.0	15.0
Vel-x 1-sigma (m/s)	0.0005	0.0010	0.0001	0.0050
Vel-y 1-sigma (m/s)	0.0005	0.0010	0.0001	0.0050
Vel-z 1-sigma (m/s)	0.0005	0.0010	0.0001	0.0050

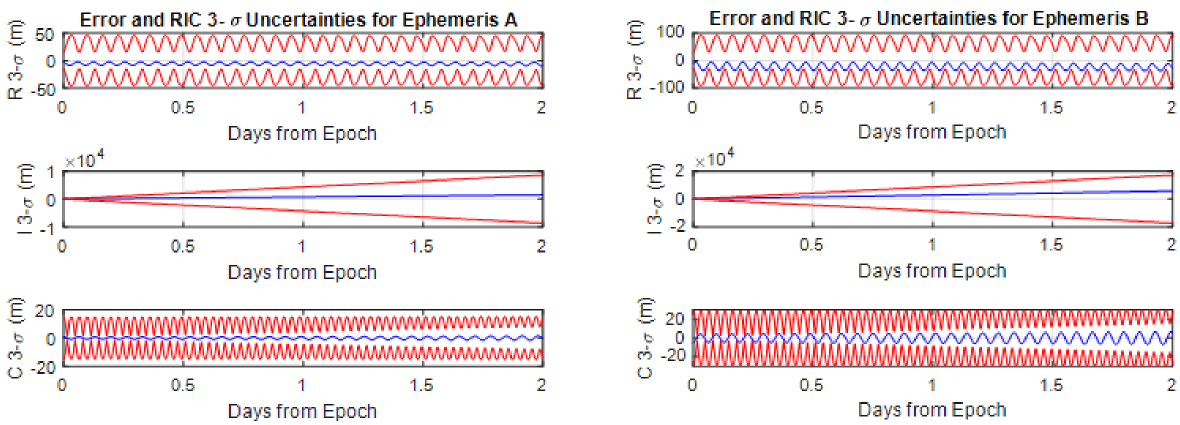

Fig. 3: Nominal Satellite-1 ephemeris A (left) vs. B (right) errors (blue) vs. 3-σ error bounds (red)

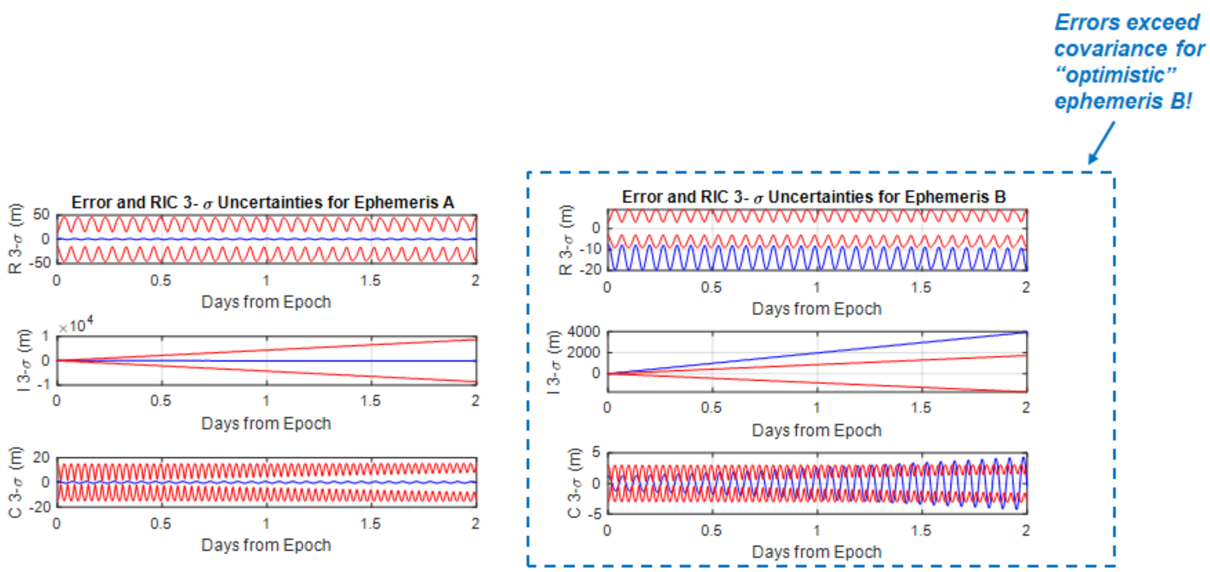

Fig. 4: Optimistic Satellite-1 ephemeris A (left) vs. B (right) errors (blue) vs. 3-σ error bounds (red)

One method is to examine the consistency between the two ephemerides A and B computed with different models which can be calculated using the Mahalanobis Distance (MD) metric as:

$$\kappa^2 = (\bar{x}_A - \bar{x}_B)^T (P_A + P_B)^{-1} (\bar{x}_A - \bar{x}_B) \tag{1}$$

where,

$$\bar{x}_A = \text{predicted ephemeris A}$$
$$\bar{x}_B = \text{predicted ephemeris B}$$
$$P_A = \text{predicted covariance of A}$$
$$P_B = \text{predicted covariance of B}$$

It is a measure of the differences between two states relative to their combined covariances. If the MD is "small" then the differences are consistent with the combined covariances, and the predictions of each covariance are deemed to be in line with their respective covariances. However, if the MD is large, the differences are inconsistent and at least one of the covariances is not consistent with their respective prediction. The MD metric is shown in Fig. 5 for ephemeris A vs. B for the nominal (left) and optimistic (right) cases. It can be seen that the optimistic MD comparison is somewhat larger than the nominal indicating an inconsistency with one of the ephemeris states and covariances. But, how does one determine the inconsistent prediction? Additional tests or another predicted state and covariance from a third source, would be needed to help identify the inconsistent prediction.

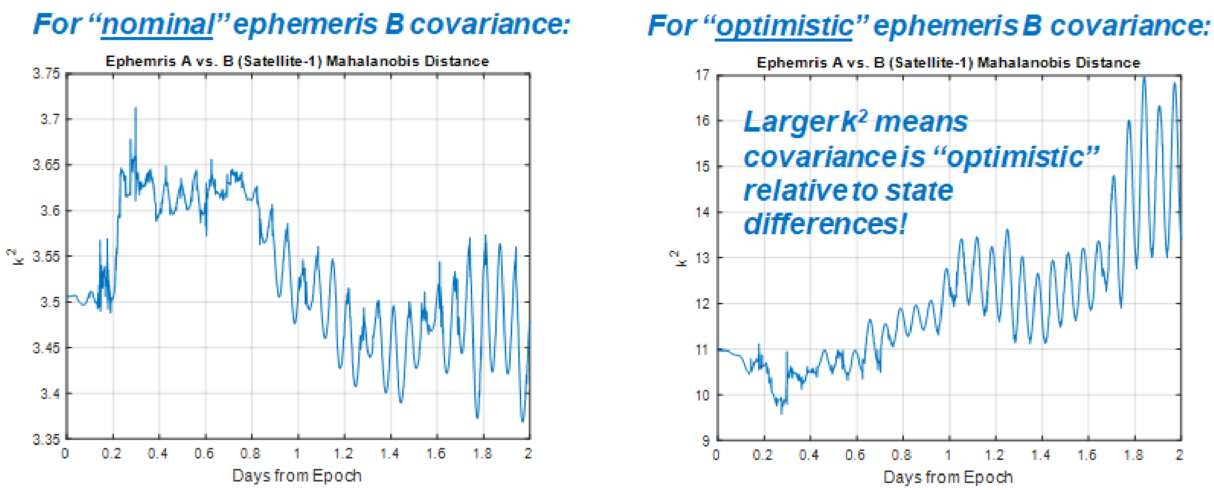

Fig. 5: Mahalanobis Distance metric for nominal (left) vs. optimistic covariance for ephemeris B

The main point to be made with this exercise is that, if two ephemeris predictions for a given satellite use two different density models, one would encounter similar inconsistencies in the predictions. If the probability of collision between Satellite-1 and Satellite-2, Pc [14], is computed using the nominal vs. optimistic predicted state differences and covariances, the optimistic case results in several orders of magnitude reduction in the likelihood of collision as summarized in Table 3 where the left-hand column represents the Pc results generated using the "nominal" ephemeris B covariance, while the right-hand column represents Pc results using the "optimistic" covariance B. The noteworthy difference is the orders of magnitude reduction of Pc for the optimistic covariance B due to the erroneous order of magnitude uncertainty for that ephemeris. The "truth" results in Table 3 also show a difference, though much smaller, for use of the ephemeris B in the Pc computation.

3. PROBABILISTIC DENSITY MODELS

This paper uses the recently developed HASDM-ML [15] and MSIS-UQ [16] atmospheric density models for orbital state and uncertainty propagation. HASDM-ML and MSIS-UQ are probabilistic machine-learning models. They leverage the "negative logarithm of predictive density (NLPD)" loss function and representative power of neural networks

Table 3: Pc for the Satellite-1 and Satellite-2 conjunction computations for nominal vs. optimistic ephemeris B

"Nominal" Ephemeris B Covariance	"Optimistic" Ephemeris B Covariance
Predicted Sat-1a vs. Sat-2: Time of conjunction = 172798.000000 sec Conjunction distance = 4.311104 km Pc = 7.847196e-04	Predicted Sat-1a vs. Sat-2: Time of conjunction = 172798.000000 sec Conjunction distance = 4.311104 km Pc = 7.847196e-04
Predicted Sat-1b vs. Sat-2: Time of conjunction = 172796.000000 sec Conjunction distance = 8.167273 km Pc = 2.538737e-04	Predicted Sat-1b vs. Sat-2: Time of conjunction = 172798.000000 sec Conjunction distance = 8.153437 km Pc = 4.711837e-09
Truth Sat-1 vs. Sat-2: Time of conjunction = 172798.000000 sec Conjunction distance = 2.232668 km Pc_a = 1.382090e-03 Pc_b = 1.163810e-03	Truth Sat-1 vs. Sat-2: Time of conjunction = 172798.000000 sec Conjunction distance = 2.232668 km Pc_a = 1.382090e-03 Pc_b = 1.453861e-03

to estimate accurate mean atmospheric density values while simultaneously predicting well-calibrated associated standard deviations.

HASDM [4] is a state-of-the-art density estimation framework used by the United States Space Force (USSF) for operational purposes. The HASDM framework uses the observed drag effects on a large number of calibration satellites (approximately 75) to make near real-time corrections to the JB2008 [17] density estimates. However, the HASDM data/model assimilation system is not directly accessible to the broader scientific community, limiting its utilization. Space Environment Technologies (SET), who is a co-developer of JB2008, does weekly validations and archiving of the HASDM output. Recently, SET has made public the so-called "SET HASDM density database" [18]. It consists of 20 years of HASDM density outputs spanning 2000 through 2019, i.e. solar cycles 23 and 24, at a cadence of 3 hours. For each epoch, density values are available over a global 12,312-dimensional grid system consisting of 27 altitudes (175-825 km at a resolution of 25 km), 19 latitudes (resolution of 10°), and 24 longitudes (resolution of 15°). The HASDM-ML surrogate model is based on the SET HASDM density database. The model takes in as input a set of 28 variables, consisting of eight solar drivers (variants of F_{10}, S_{10}, M_{10}, and Y_{10} indices), sixteen geomagnetic drivers (variants of a_p and Dst indices), and four temporal drivers (trigonometric functions of the epoch under consideration); for more details on the inputs, interested readers can refer to [15].

The latest atmospheric density model in the well-known "Mass Spectrometer and Incoherent Scatter radar (MSIS)" family is the Naval Research Laboratory (NRL) MSIS 2.0 [19]. In work by Licata et al. [16], the authors develop a machine learning-based stochastic exospheric temperature model, which is then fed into NRLMSIS 2.0 to get probabilistic MSIS-UQ density outputs. MSIS-UQ is based on an exospheric temperature database with close to 81 million samples. These exospheric temperatures are obtained using a binary search method [20–22] such that the densities from NRLMSIS 2.0 match high-fidelity density estimates of the CHAMP, GRACE-A, Swarm A, and Swarm B satellites. The input variables for the MSIS-UQ model consist of 21 space weather, spatial, and temporal parameters, the details of which can be found in [16].

The motivation behind including multiple density models (HASDM-ML and MSIS-UQ) in this analyses is to ensure diversity of representation. The two models are associated with different base empirical models (JB2008 vs NRLMSIS 2.0) and different sources of satellite data/cadence. A thorough comparison between the performance of HASDM-ML and MSIS-UQ can be found in [16]. Both orbit uncertainty evolution and critical SSA by-products, such as the Pc are functions of the density model selected.

4. ERROR PROPAGATION FOR SPATIO-TEMPORAL CORRELATION PRESERVATION

For orbit uncertainty propagation provided in the Results section, a Monte Carlo approach is utilized, as it can capture the higher-order moments beyond the mean and covariance. For the 'traditional' Monte Carlo approach [23] to studying the effect of atmospheric density uncertainty, values of atmospheric density are sampled from the stochastic density models at frequent intervals along the orbital path. The frequent sampling partially "cancels" or "balances" the orbital drag perturbations, and this results in orbital errors that are unrealistically small and not representative of actual physical behavior. A hypothetical example would be density sampling from a normal distribution $\mathcal{N}(10^{-12}kg/m^3, 10^{-13}kg/m^3)$ (assuming the distribution is approximately constant for a short time scale). At 1s cadence, sampled density values at subsequent time steps can be $.94 \times 10^{-12}kg/m^3$, $1.07 \times 10^{-12}kg/m^3$, $.98 \times 10^{-12}kg/m^3$, and $1.01 \times 10^{-12}kg/m^3$, respectively. The along-track drag effects, with respect to the orbit propagated with mean density, partially cancel between densities larger and smaller than the mean value. This behavior is demonstrated in Figs. 4(a) and 4(b) of [23]. In other words, the traditional Monte Carlo approach does not account for the spatio-temporal correlation among the density values of neighboring locations or epochs in orbit.

To preserve the spatio-temporal correlation, a modified Monte Carlo technique based on the first-order Gauss-Markov process is used, which is a well-known stochastic process that "obeys the Gaussian probability law and displays the Markov property" [24]. In this modified scheme, a bias factor κ_0 is sampled from the standard normal distribution at $t = 0$, which represents the initial epoch. Density at $t = 0$ is then given as $\rho_{t=0} = \mu_{t=0} + \kappa_0 \sigma_{t=0}$, where the density mean $\mu_{t=0}$ and standard deviation $\sigma_{t=0}$ are obtained from the stochastic atmospheric density model(s). At all other subsequent time steps during the orbit propagation, the bias factor is computed as [24]:

$$\kappa(t+\Delta t) = \exp(-\beta \Delta t)\kappa(t) + u_k(t+\Delta t)\sqrt{\frac{\sigma^2}{2\beta}\left(1-\exp(-2\beta\Delta t)\right)} \tag{2a}$$

$$\beta = -\frac{\ln 0.5}{\tau} \tag{2b}$$

where $u_k(t+\Delta t)$ is a sampled number from the standard normal distribution, the factor $(\sigma^2/(2\beta))$ (steady-state variance of κ) is taken as 1, and the parameter τ represents the "half-life", which governs the rate at which the auto-correlation fades. At each time step, the density is computed as $\rho_{t+\Delta t} = \mu_{t+\Delta t} + \kappa(t+\Delta t)\sigma_{t+\Delta t}$, which is then fed into the dynamical model. For these investigations, the half-life is taken as 18 minutes based on the analysis carried out in Fig. 4 of [23].

5. PROBABILITY OF COLLISION (Pc) COMPUTATIONS

In the early days when the near-Earth space environment was relatively less populated, conjunction assessments often relied on miss distance at the Time of Closest Approach (TCA) [25]. However, as the satellite and debris population grew and the importance of SSA and STM increased, this basic metric became inadequate. Over time, the probability of collision (Pc), which represents the likelihood of two space objects colliding, emerged as a widely adopted metric for assessing conjunction threats among satellite operators and the scientific community. The popularity of Pc as a metric can be attributed to its ease of interpretation, the tractability of calculation, and rigorous theoretical underpinning, drawing upon several variables such as the miss distance, uncertainty distributions of the conjunction objects, and the physical sizes (or a user-defined threshold) of the two objects. Despite the popularity, the Pc estimate is only as good as the reliability of the estimated uncertainties. Unrealistic uncertainty estimates leading to too small a covariance ("robust region" [26]) can lead to unnecessary maneuvers, resulting in excessive expenditure of fuel. Similarly, unrealistic uncertainty estimates leading to too large a covariance ("dilution region" [26]) can lead to the disregard of actual high-risk events. This paper investigates Pc using two techniques - (1) the Brute Force Monte Carlo (BFMC) method [27] and (2) Foster's 2D method [14, 28].

The BFMC algorithm [27] for Pc estimation is a high-fidelity Special Perturbations (SP) orbit propagation-based approach. Let n_{BFMC} be the number of Monte Carlo trials. For each trial, the initial states (assuming an estimate of initial state uncertainty) are sampled for the primary and secondary objects. The two initial states are propagated using the SP dynamical model, accounting for density uncertainty (if modeled) implemented using the first-order Gauss-Markov process, to obtain the states at time t: $\mathbf{r}_{1k}(t)$ and $\mathbf{r}_{2k}(t)$. The subscript k stands for the k^{th} trial and it is assumed that the initial epoch is the same for both objects (this constraint can easily be relaxed). The distance between the two objects at a general time t is given as:

$$\mathbf{r}_{12,k}(t) = |\mathbf{r}_{1k}(t) - \mathbf{r}_{2k}(t)| \tag{3}$$

where $|\cdot|$ is the l_2-norm. Of interest is the risk assessment in a band of time around the TCA: $TCA - (T_B/2) \leq t \leq TCA + (T_B/2)$, where T_B is the length of the period of interest. Assuming a user-defined "threshold" of λ, the k^{th} trial is assumed to result in a collision or contact if the minimum value of $\mathbf{r}_{12,k}(t)$ during the period of interest satisfies:

$$min(\mathbf{r}_{12,k}(t)) \leq \lambda \quad ; \quad TCA - \frac{T_B}{2} \leq t \leq TCA + \frac{T_B}{2} \tag{4}$$

A collision/contact counter $N_c(TCA-(T_B/2), TCA+(T_B/2))$ is initiated to 0 before the first trial is simulated. This counter is incremented by 1 every time a collision/contact happens, i.e., every time a trial satisfies Eq. (4). After all the trials are simulated, the probability of collision is estimated as:

$$\text{Pc} = \frac{N_c(TCA-(T_B/2), TCA+(T_B/2))}{n_{BFMC}} \tag{5}$$

Foster's 2D method for Pc computation is an approximate semi-analytic technique, which relies on the following assumptions [14, 28, 29]:

1. The relative satellite motion during the conjunction is approximated as linear, i.e., the effect of relative acceleration on the motion is ignored.
2. The uncertainties in the velocities of the primary and secondary objects are ignored. The uncertainties in the positions of the primary and secondary objects are zero-mean, Gaussian, and uncorrelated during the conjunction.
3. The relative position uncertainty is constant during the conjunction
4. Both the primary and secondary objects have spherical shapes

Foster's 2D Pc is computed by projecting the 3D position probability density function (PDF) onto the encounter plane, which is perpendicular to the relative velocity vector. Let, $\mathbf{r}_i$, $\mathbf{v}_i$, and P_i $(i=1,2)$ represent the Earth-centered inertial (ECI) position, velocity, and covariance matrix, respectively, of the two objects at the TCA. The combined position covariance in the ECI frame is then obtained as: $P = P_1 + P_2$. The covariance P is then projected onto the encounter plane using the following transformations [30]:

$$\tilde{P} = \tilde{A} P \tilde{A}^T \tag{6a}$$

$$P_p = \begin{bmatrix} 1 & 0 & 0 \\ 0 & 0 & 1 \end{bmatrix} \tilde{P} \begin{bmatrix} 1 & 0 & 0 \\ 0 & 0 & 1 \end{bmatrix}^T \tag{6b}$$

where $\tilde{A}$ is the matrix for transformation from the ECI to the relative encounter frame (REF), which is defined as:

$$REF_y = \frac{\mathbf{v}_1 - \mathbf{v}_2}{|\mathbf{v}_1 - \mathbf{v}_2|} \tag{7a}$$

$$REF_z = \frac{(\mathbf{r}_1 - \mathbf{r}_2) \times (\mathbf{v}_1 - \mathbf{v}_2)}{|(\mathbf{r}_1 - \mathbf{r}_2) \times (\mathbf{v}_1 - \mathbf{v}_2)|} \tag{7b}$$

$$REF_x = REF_y \times REF_z \tag{7c}$$

where the subscripts 1 and 2 correspond to the primary and secondary objects, respectively. The 2D Pc is then computed as [30]:

$$Pc = \frac{1}{2\pi\sqrt{||P_p||}} \int_{x0-HBR}^{x0+HBR} \int_{-\sqrt{HBR^2-(x-x0)^2}}^{\sqrt{HBR^2-(x-x0^2)}} EXP\left(-\frac{1}{2}\left(\tilde{C}_{11}x^2 + \tilde{C}_{12}zx + \tilde{C}_{21}zx + \tilde{C}_{22}z^2\right)\right) dzdx \tag{8a}$$

where $\tilde{C}_{ij}$ are the elements of the matrix $\tilde{C} = P_p^{-1}$, hard-body radius HBR is the combined object radius, $||P_p||$ is the determinant of matrix P_p, EXP is the exponential function, and $x0 = |\mathbf{r}_1 - \mathbf{r}_2|$.

6. RESULTS AND DISCUSSION

To investigate the effects of realistic uncertainty modeling and highlight the importance of space weather conditions, several simulation experiments are designed involving two LEO satellites at an altitude of approximately 500 km. The first satellite is inspired by SpaceX's Starlink satellite constellation, and the second satellite is inspired by Planet's Dove satellite constellation. These satellites are referred to as Sat-X and Sat-D throughout this section, respectively. The mass, cross-sectional area, drag coefficient, and ballistic coefficient for the two satellites are listed in Table 4. Sat-X has roughly 43° inclination, Sat-D has roughly 98° inclination, and both satellites have near-zero eccentricity. The 'reference' states in the ECI coordinate system for the two satellites are given in Table 5. The distance between the reference states of the two satellites is approximately 50 meters. The epoch E_s corresponding to the reference states in Table 5 is taken as 2452524.54167 JD (01:00:00 UT on September 7, 2002), which marks the main phase onset of a large geomagnetic storm [31]. The reference states at epoch E_s are back-propagated to obtain the 'initial' states. The back-propagation parameters are given in Table 6, where only the mean values of the HASDM-ML density model are used. The initial states are given in Table 7. Note that the objects and orbits investigated here are similar, but not the same, to those considered in the motivating example section.

Table 4: Sat-X and Sat-D ballistic coefficient parameters

Parameters	Sat-X	Sat-D
Mass m (kg)	185	5.8
Cross-Sectional Area A (m^2)	5	0.08639379797371934
Drag Coefficient C_D	2.2	2.2
Ballistic Coefficient $BC = \frac{C_D A}{m}$ (m^2/kg)	0.05945945945945946	0.0327700613003763

Table 5: Sat-X and Sat-D reference states in the Cartesian coordinate system

State Element	Sat-X Reference State	Sat-D Reference State
Pos-x (km)	3983.525467946707	3983.534443678169
Pos-y (km)	-3174.742802645622	-3174.783908594208
Pos-z (km)	4618.142025687412	4618.114998623155
Vel-x (km/s)	4.045879885471127	-4.820263295703204
Vel-y (km/s)	6.388364271355713	2.012311813015446
Vel-z (km/s)	0.901780056946159	5.541580159923150

Table 6: Backpropagation simulation parameters for obtaining the initial states

Simulation Parameter	Value/Details
Perturbation Forces	Earth gravity higher order harmonics up to degree and order 12 (EGM96), Sun gravity, Moon gravity, atmospheric drag, cannonball-based solar radiation pressure
Atmospheric Density Model	HASDM-ML (mean)
Integrator	Dormand and Prince's Runge-Kutta (4,5) ordinary differential equation (ODE) solver [32] with relative and absolute tolerance of 10^{-10}
Back-propagation Duration	172800 seconds (2 days)
Object Shape	Uniformly spherical

Next, using the initial states listed in Table 7, Monte Carlo simulations are carried out for forward orbit uncertainty propagation over a duration of three days. The details of the simulation cases are given in Table 8. Four space weather conditions are considered - a case where the space weather is quiet (SW1 or 'quiet case') and three cases with a geomagnetic storm (SW2, SW3, SW4). For the 'storm Day 2 case' (SW2), the geomagnetic storm starts at the end of the second day of orbit propagation. For the 'storm Day 1 case' (SW3), the geomagnetic storm starts at the end of the first day of orbit propagation. For the 'storm Day 0 case' (SW4), the geomagnetic storm starts at

Table 7: Sat-X and Sat-D initial states in the Cartesian coordinate system

State Element	Sat-X Initial State	Sat-D Initial State
Pos-x (km)	-5014.1074100656	-766.142671682041
Pos-y (km)	602.8300754941	1623.61810917883
Pos-z (km)	-4674.73278075828	-6646.91562916332
Vel-x (km/s)	-1.32966729434151	6.31925159218635
Vel-y (km/s)	-7.47740528421353	-3.87917514517977
Vel-z (km/s)	.463184768105425	-1.66660405141095

the beginning of orbit propagation. It is difficult to predict space weather conditions in advance, so one may think of the four simulated space weather conditions as investigating the outcome/cost of wrong space weather prediction. For example, the predictions may indicate that the space weather condition for the next three days is quiet, but a geomagnetic storm may start at the end of the second day, possibly resulting in a conjunction scenario very different from the prediction. For each space weather condition, two uncertainty scenarios are investigated: under the U1 scenario, just the initial orbital state uncertainty is considered, and under the U2 scenario, both the initial orbital state uncertainty and the atmospheric density uncertainty are considered. The difference between the two uncertainty scenarios could be viewed as investigating the cost of ignoring atmospheric density uncertainty. For each space weather condition (SW1/SW2/SW3/SW4) and uncertainty scenario (U1/U2), two atmospheric density models are considered: under the A1 scheme, both Sat-X and Sat-D are propagated using the HASDM-ML model, and under the A2 scheme, both satellites are propagated using the MSIS-UQ model. For each density model, there needs to be a corresponding drag coefficient value. The MSIS-UQ model is thus 'debiased' w.r.t the HASDM-ML model using the past two days of density data. The debiasing is explained in italics in more detail: *for each space weather condition, the satellite (Sat-X/Sat-D) is back-propagated from the initial epoch for two days using HASDM-ML mean density values. At each location/epoch along this back-propagated path, the ratio between HASDM-ML and MSIS-UQ mean density values is computed. The average value of all such ratios is then computed and used to scale the drag coefficient corresponding to the MSIS-UQ, i.e.,* $CD_{MSIS-UQ} = (\rho_{HASDM}/\rho_{MSIS-UQ})_{avg} CD_{HASDM}$*, where* $CD_{HASDM} = 2.2$. The sizes of the covariance matrices listed in Table 8 are representative of typical initial orbit determination (IOD) results obtained from onboard Global Positioning System (GPS) measurements. The Monte Carlo trials are carried out using the same dynamical model (perturbation forces) and numerical integrator as those listed earlier in Table 6.

Table 8: Orbit uncertainty propagation - simulation details

Simulation Parameters	Value/Details
Space Weather Conditions	(SW1) 'quiet case': initial epoch = 2455165.5 JD (00:00:00 UT on November 30, 2009), (SW2) 'storm Day 2 case': initial epoch = 2452522.54167 JD (01:00:00 UT on September 5, 2002), (SW3) 'storm Day 1 case': initial epoch = 2452523.54167 JD (01:00:00 UT on September 6, 2002), (SW4) 'storm Day 0 case': initial epoch = 2452524.54167 JD (01:00:00 UT on September 7, 2002)
Atmospheric Density Model	(A1) HASDM-ML, (A2) 'debiased' MSIS-UQ
Uncertainties Considered	(U1) Only initial orbital state uncertainty, (U2) Both initial orbital state uncertainty and atmospheric density uncertainty
Orbit Propagation Duration	259200 seconds (3 days)
Number of Monte Carlo Trials	1000
Initial Uncertainty (Covariance Matrix) for Sat-X	Diagonal[5^2 m^2, 5^2 m^2, 5^2 m^2, 0.0005^2 $(m/s)^2$, 0.0005^2 $(m/s)^2$, 0.0005^2 $(m/s)^2$]
Initial Uncertainty (Covariance Matrix) for Sat-D	Diagonal[14^2 m^2, 14^2 m^2, 14^2 m^2, 0.05^2 $(m/s)^2$, 0.05^2 $(m/s)^2$, 0.05^2 $(m/s)^2$]

Fig. 6 shows the orbital state uncertainty distribution at the TCA with only the initial orbital state uncertainty considered. The TCA is computed based on the propagated mean initial states with mean density values along the orbital trajectory. The magenta Monte Carlo samples correspond to the Sat-X satellite, and the cyan samples correspond to the Sat-D satellite. The estimated mean positions are shown using asterisks. Figs. 6a and 6b correspond to the 'quiet case' space weather condition with each propagation carried out using HASDM-ML mean and MSIS-UQ mean atmospheric density models, respectively. Similarly, Figs. 6c, 6d correspond to the 'storm Day 2 case', Figs. 6e, 6f correspond to the 'storm Day 1 case', and Figs. 6g, 6h correspond to the 'storm Day 0 case'. The title of the individual figures provides the miss distance and the TCA information. The closest approach is estimated at 172800 s (2 days) for the 'storm Day 2' and 'storm Day 1' cases, at 184170 s (2.13 days) for the 'quiet case', and at 169960 s (1.97 days) for the 'storm Day 0 case'. In other words, if one predicts a geomagnetic storm at the end of the first or second day but encounters an unexpectedly quiet space weather condition or a geomagnetic storm that starts right at the beginning of orbit propagation, the TCA may shift in either direction. The estimated miss distance between Sat-X and Sat-D satellites is a function of both the future space weather condition and the atmospheric density model one uses, even if appropriate debiasing is carried out. For less active space weather conditions, the difference between HASDM-ML and MSIS-UQ is less prominent, resulting in similar miss distances: 9915.52 m versus 9921.99 m for the 'quiet case'. Generally speaking, it is easier to capture space weather variations during quiet times, and as a result, most density models differ in their predictions during active space weather conditions. For very close encounters during storm time, the selection of the density model becomes critical – for 'storm Day 2 case', HASDM-ML gives a miss distance of approximately 50 m, whereas MSIS-UQ gives a miss distance of approximately 1400 m, which is an order of magnitude higher than that of the HASDM-ML model. Instead of the storm starting at the end of the second day, if the storm starts at the end of the first day, the miss distance estimates increase to 5889.54 m and 4304.95 m for HASDM-ML and MSIS-UQ mean models, respectively. Finally, if the storm starts at the beginning of orbit propagation, the cumulative effect of the storm-time mismatch between the two density models can result in very different miss distances: 42802.49 m for HASDM-ML mean model and 23084.10 m for MSIS-UQ mean model. From the spread of Monte Carlo samples in Fig. 6, in-track position uncertainty is the most important contributor to the overall position uncertainty distribution. The in-track position uncertainty at the TCA is distinctly larger for the Sat-D satellite (cyan samples) when compared to the Sat-X satellite (magenta samples), mainly because the Sat-D satellite started with a larger initial covariance matrix. If the initial covariance matrices were larger, representative of some ground-based/low-budget measurement sensors, one may see the 'linear banana (a thin and elongated banana)' position uncertainty distribution.

To quantify the effect of the propagated uncertainties shown in Fig. 6, the Pc is computed using the BFMC method and present it in Fig. 7. The BFMC Pc is calculated for the duration $[TCA-3H, TCA+3H]$. Pc is calculated for various threshold values: [50 m, 100 m, 500 m, 1 km, 5 km, 10 km, 20 km, 30 km, 50 km, 100 km]. Figs. 7a and 7b show the Pc values (y-axis) in linear and log scales, respectively. The specific values of the threshold and BFMC Pc at which a satellite owner/operator (O/O) decides to take a collision-avoidance action depend on individual considerations and technological capabilities. For example, suppose a satellite O/O 1 uses MSIS-UQ mean density model and has a policy that it cannot tolerate risk of more than 0.003 for a threshold of 1 km. In that case, it may end up performing a collision avoidance maneuver if it thinks that a large storm will start at the end of the second day (corresponding Pc from Fig. 7 is 0.004995). Similarly, if another O/O 2 uses HASDM-ML mean density model, has the same risk tolerance as O/O 1, and thinks that the space weather condition is going to be quiet, it may not take any action (corresponding Pc from Fig. 7 is 0.001998). Some O/O may prefer to use Foster's 2D method for Pc calculation. The 2D Pc values at the TCA are given in Table 9.

Next, Fig. 8 shows the orbital state uncertainty distribution at the TCA when both initial orbital state uncertainty and the atmospheric density uncertainty are considered. In maroon, the Sat-X Monte Carlo samples are shown; in green, the Sat-D Monte Carlo samples are shown. For comparison, the samples corresponding to the cases when only initial orbital state uncertainty is considered (these samples are shown in violet for Sat-X and cyan for Sat-D) are also provided. The effect of atmospheric density uncertainty on the spread of the Monte Carlo samples is minimal for the 'quiet case' (Figs. 8a, 8b). For the Sat-X satellite, atmospheric density uncertainty results in a larger spread in the Monte Carlo samples during storm times (compared to the scenarios where only initial orbital state uncertainty is considered). This is particularly evident in the 'storm Day 0 case' (Figs. 8g, 8h), mainly because the satellite was inside a geomagnetic storm for a longer period resulting in a greater cumulative effect.

Corresponding to the distributions shown in Fig. 8 resulting from initial orbital state and density uncertainties, Pc is computed and presented in Fig. 9 and Table 10. Figs. 9a and 9b show the computed BFMC Pc (for $[TCA-3H, TCA+3H]$ window) in linear and log scales, respectively. For comparison, the BFMC Pc values corresponding to the cases when only initial orbital state uncertainty is considered are shown. Solid lines correspond to the scenarios where both initial and density uncertainties are considered; dashed lines correspond to the scenarios where only initial orbital state uncertainty is considered. The effect of the inclusion of density uncertainty on BFMC Pc value is a function of space weather conditions, the density model used, and the threshold value. Table 10, presents the Pc values computed using

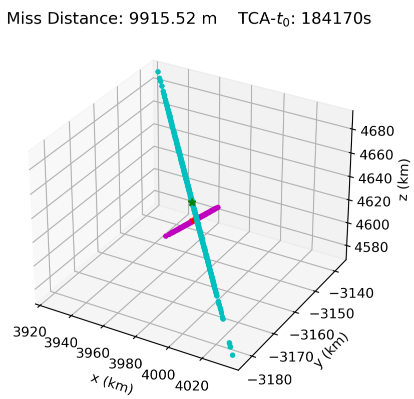

(a) ‘Quiet case’, HASDM-ML mean

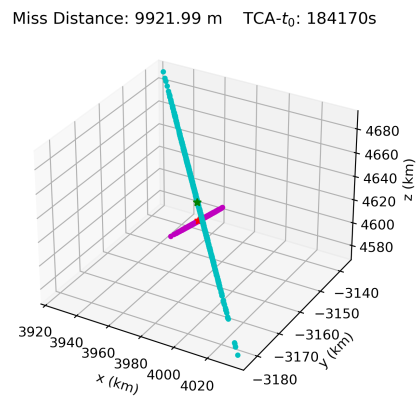

(b) ‘Quiet case’, MSIS-UQ mean

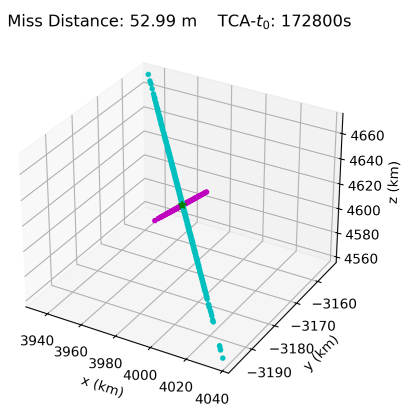

(c) ‘Storm Day 2 case’, HASDM-ML mean

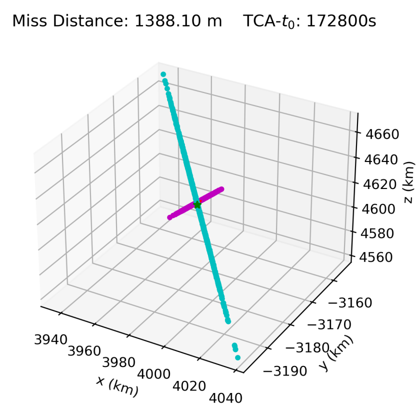

(d) ‘Storm Day 2 case’, MSIS-UQ mean

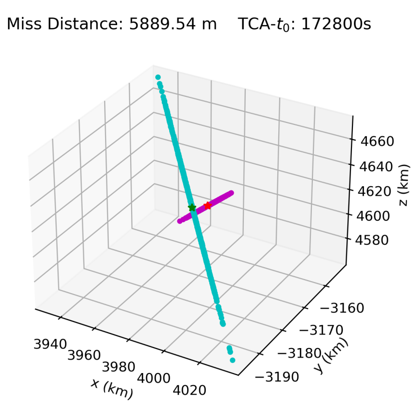

(e) ‘Storm Day 1 case’, HASDM-ML mean

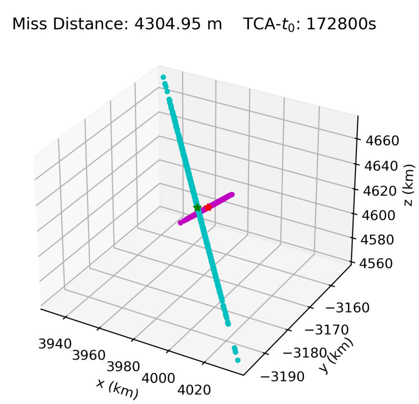

(f) ‘Storm Day 1 case’, MSIS-UQ mean

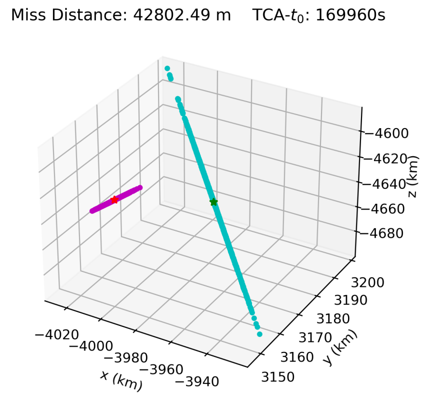

(g) ‘Storm Day 0 case’, HASDM-ML mean

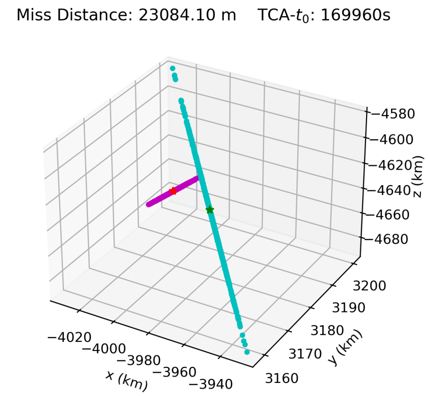

(h) ‘Storm Day 0 case’, MSIS-UQ mean

Fig. 6: Orbital state uncertainty distribution at the TCA. In magenta, the Sat-X samples, and in cyan, the Sat-D samples. Only initial orbital state uncertainty is considered

Table 9: Pc for the quiet and storm cases obtained using Foster’s 2D method, where the HBR/threshold is taken as the summation of the radii of the two objects. Only initial orbital state uncertainty is considered

Scenario	2D Pc
‘Quiet case’, HASDM-ML mean	5.5286E-10
‘Quiet case’, MSIS-UQ mean	5.6964E-10
‘Storm Day 2 case’, HASDM-ML mean	7.5924E-07
‘Storm Day 2 case’, MSIS-UQ mean	6.8317E-07
‘Storm Day 1 case’, HASDM-ML mean	7.3851E-12
‘Storm Day 1 case’, MSIS-UQ mean	1.2668E-20
‘Storm Day 0 case’, HASDM-ML mean	0
‘Storm Day 0 case’, MSIS-UQ mean	0

Foster’s 2D method. Comparison between Table 10 (initial+density uncertainties) and Table 9 (only initial uncertainty) highlights that the largest change happens in the ‘storm Day 1’ case, where the 2D Pc values are an order of magnitude higher when density uncertainty is included. For the important ‘storm Day 2 case’, which has relatively high 2D Pc values (order of 10^{-7}), the inclusion of atmospheric density uncertainty reduces the collision probability for both HASDM-ML and MSIS-UQ density models.

Table 10: Pc for the quiet and storm cases obtained using Foster’s 2D method, where the HBR/threshold is taken as the summation of the radii of the two objects. Both initial orbital state uncertainty and density uncertainty are considered

Scenario	2D Pc
‘Quiet case’, HASDM-ML	5.5178E-10
‘Quiet case’, MSIS-UQ	6.9790E-10
‘Storm Day 2 case’, HASDM-ML	7.5379E-07
‘Storm Day 2 case’, MSIS-UQ	6.6014E-07
‘Storm Day 1 case’, HASDM-ML	1.1696E-11
‘Storm Day 1 case’, MSIS-UQ	3.0374E-19
‘Storm Day 0 case’, HASDM-ML	0
‘Storm Day 0 case’, MSIS-UQ	0

For a select few scenarios, the breakdown of normality is investigated, which may impact important SSA and STM applications that rely on the assumption that the errors follow a Gaussian distribution. The D’Agostino and Pearson’s

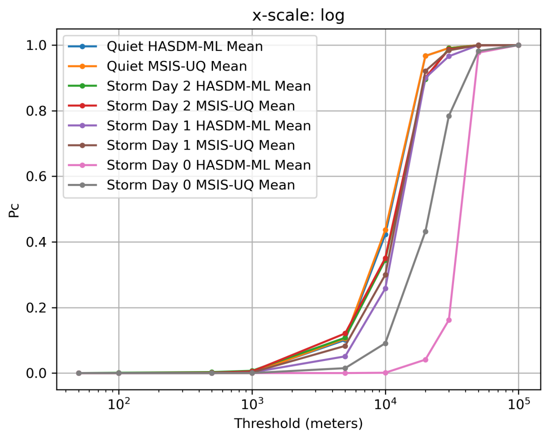

(a) BFMC Pc (y-axis: linear scale)

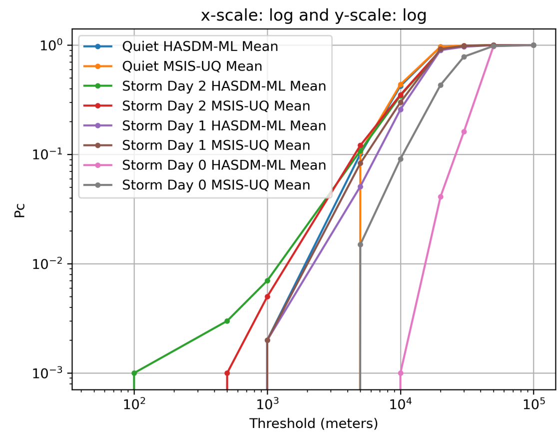

(b) BFMC Pc (y-axis: log scale)

Fig. 7: Pc for the quiet and storm cases obtained using the BFMC method for the duration $TCA \pm 3H$. Only initial orbital state uncertainty is considered. In sub-figure (a), Pc is shown in linear scale, and in (b), Pc is shown in logarithmic scale

"normal test" [33, 34] are used, which combines measures of skewness and kurtosis to generate an omnibus test for normality (and available through Python's SciPy library [35] (*scipy.stats.normaltest*)). Fig. 10 shows the time history of p-values computed for Sat-D ECI position components (x, y, z). The results correspond to scenarios where both initial orbital state uncertainty and density uncertainty from the HASDM-ML model are considered. Figs. 10a, 10b, 10c, and 10d correspond to the 'quiet', 'storm Day 2', 'storm Day 1', and 'storm Day 0' cases, respectively. A reference p-value of .01 is assumed, which is shown in red. Let H_0 be the hypothesis that the observed data comes from a normal distribution, and let H_1 be the alternative hypothesis that the observed data does not come from a normal distribution. P-values smaller than the threshold .01 indicate strong evidence in support of hypothesis H_1, i.e., the observed data does not come from a normal distribution. Whereas p-values greater than or equal to the threshold .01 imply that one cannot reject the hypothesis H_0 (not the same as accepting hypothesis H_0). Fig. 10 illustrates strong evidence the errors are not Gaussian (p<.01 values) starts emerging beyond roughly 10 hours. An example application of this information would be sensor tasking. If an operator of some sensor(s) relies on the use of a Kalman filter derivative, including the Extended or Unscented varieties, they would do well to implement a sensor tasking algorithm for re-observation of objects before the p-values are estimated to fall below the user-defined threshold. This

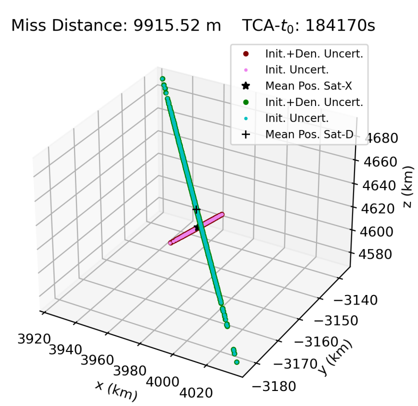

(a) 'Quiet case', HASDM-ML

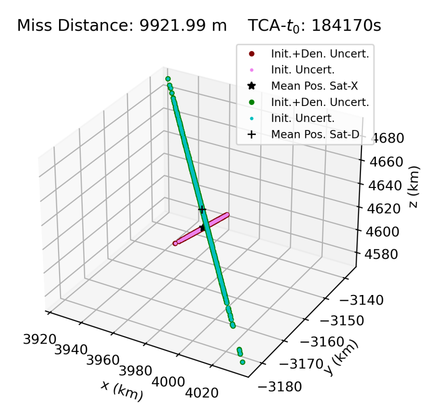

(b) 'Quiet case', MSIS-UQ

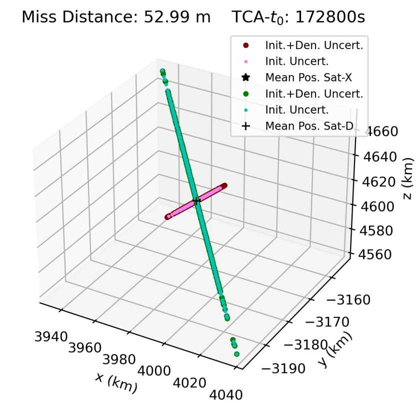

(c) 'Storm Day 2 case', HASDM-ML

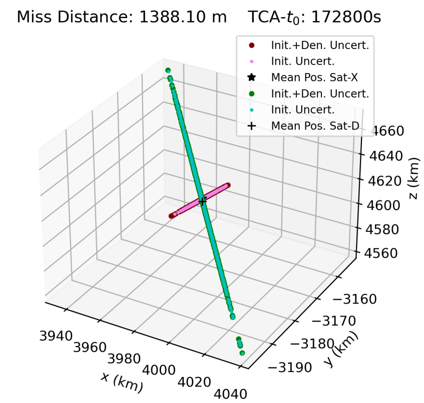

(d) 'Storm Day 2 case', MSIS-UQ

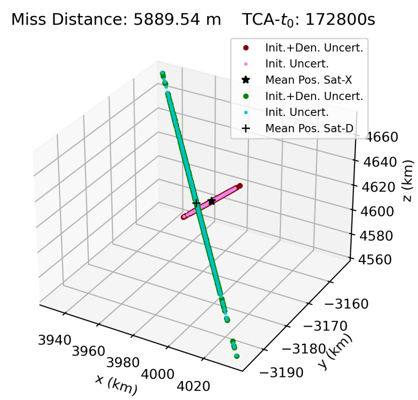

(e) 'Storm Day 1 case', HASDM-ML

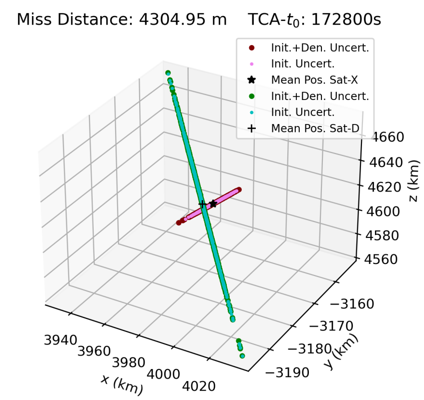

(f) 'Storm Day 1 case', MSIS-UQ

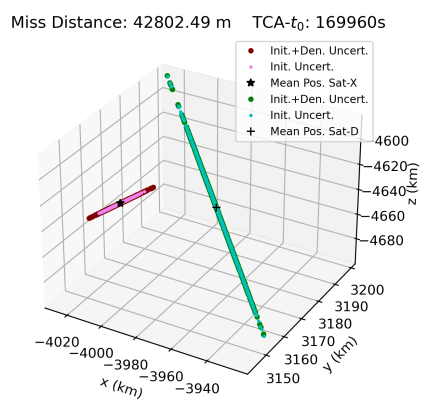

(g) 'Storm Day 0 case', HASDM-ML

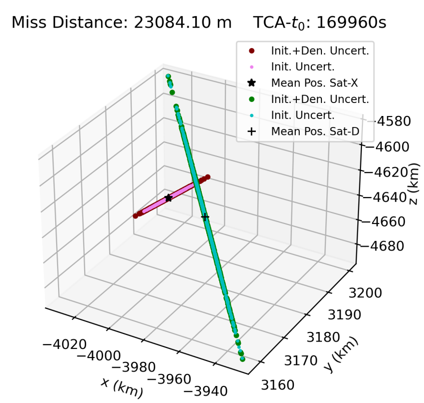

(h) 'Storm Day 0 case', MSIS-UQ

Fig. 8: Orbital state uncertainty distribution at the TCA. The maroon (Sat-X) and green (Sat-D) samples correspond to the case where both orbital state uncertainty and density uncertainty are considered. The violet (Sat-X) and cyan (Sat-D) samples correspond to the case where only initial orbital state uncertainty is considered

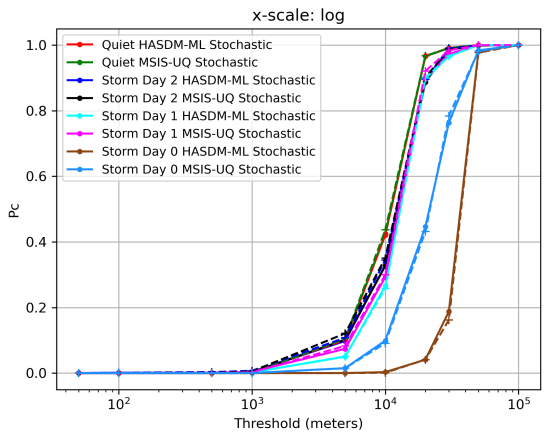

(a) BFMC Pc (y-axis: linear scale)

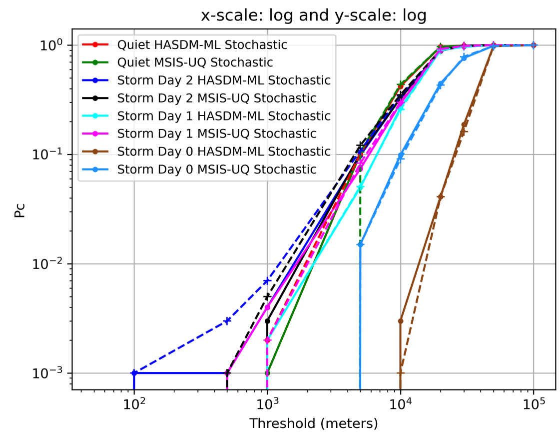

(b) BFMC Pc (y-axis: log scale)

Fig. 9: Pc for the quiet and storm cases obtained using the BFMC method for the duration $TCA \pm 3H$. Solid lines: both initial orbital state uncertainty and density uncertainty are considered. Dashed lines: only initial orbital state uncertainty is considered. In sub-figure (a), Pc is shown in linear scale, and in (b), Pc is shown in logarithmic scale

ensures that the fundamental assumptions of the data processing pipeline are not violated. The analysis shown in Fig. 10 is preliminary, and one may want to explore other metrics for testing the departure from the Gaussian assumption.

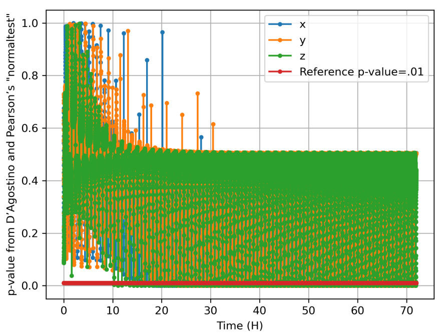

(a) 'Quiet case', HASDM-ML, Sat-D

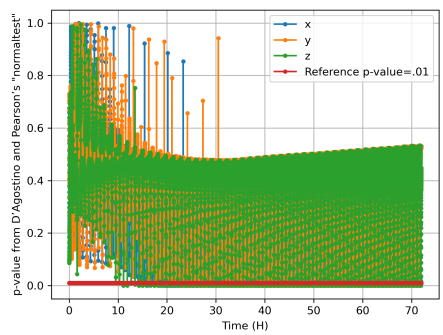

(b) 'Storm Day 2 case', HASDM-ML, Sat-D

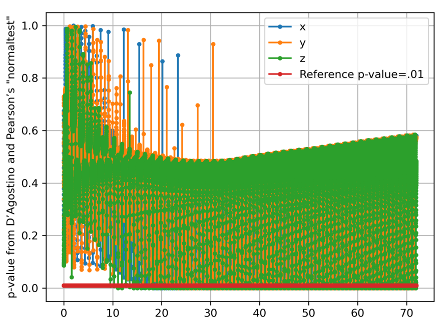

(c) 'Storm Day 1 case', HASDM-ML, Sat-D

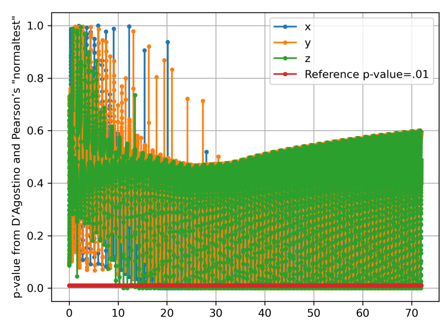

(d) 'Storm Day 0 case', HASDM-ML, Sat-D

Fig. 10: D'Agostino and Pearson's normality test for Sat-D: p-values are computed for x, y, z for quiet and storm space weather conditions. Both initial orbital state uncertainty and density uncertainty are considered.

7. CONCLUSIONS AND FUTURE WORK

This initial assessment of the HASDM-ML and MSIS-UQ show that the estimated Pc values, miss distance, and the time of closest approach varied significantly depending upon the space weather condition and the density model used. For example, the 'storm Day 2 case', the miss distance for the HASDM-ML model was approximately 50 m, which increases to roughly 1400 m for the MSIS-UQ model. One limitation of the current analysis is the number of Monte Carlo samples used, which was done for computational expediency. Future work will assess the best way to enhance the accurate of probability distribution models, either by increasing the number of samples, or by the use of sigma points-based consider covariance for orbit uncertainty propagation and Pc analysis [23]. Additionally, several of the use case Pcs are orders of magnitude lower than typical actionable thresholds. Reiterating the study with different initial states and uncertainties would allow a more complete quantification of the sensitivity of propagation errors to density model uncertainty improvements. Finally, additional methods that allow for testing of multivariate normality, such as the Henze-Zirkler test, will be used to assess how the distribution of errors evolve over the prediction timeline.

8. ACKNOWLEDGEMENTS

The authors wish to acknowledge funding received to support this work. This research is based upon work supported in part by the Office of the Director of National Intelligence (ODNI), Intelligence Advanced Research Projects Activity (IARPA), via 2023-23060200005. The views and conclusions contained herein are those of the authors and should not be interpreted as necessarily representing the official policies, either expressed or implied, of ODNI, IARPA, or the U.S. Government. The U.S. Government is authorized to reproduce and distribute reprints for governmental purposes notwithstanding any copyright annotation therein. Drs. Thomas Kelecy and Ryan Coder also thank the Space Safety Institute (SSI) at the Aerospace Corporation for providing the funding to support their contributions to this work. Lastly, the authors would like to express our heartfelt appreciation to Dr. Travis Lechtenberg at the Aerospace Corporation for his thorough and thoughtful review comments on this work.

9. REFERENCES

[1] European Space Agency. ESA's Annual Space Environment Report. LOG GEN-DB-LOG-00288-OPS-SD, ESA Space Debris Office, June 2023.

[2] Bhavya Lal, Asha Balakrishnan, Becaja M Caldwell, Reina S Buenconsejo, and Sara A Carioscia. Global trends in space situational awareness (SSA) and space traffic management (STM). *Science and Technology Policy Institute*, 2018.

[3] Theodore J. Muelhaupt, Marlon E. Sorge, Jamie Morin, and Robert S. Wilson. Space traffic management in the new space era. *Journal of Space Safety Engineering*, 6(2):80–87, 2019. doi: 10.1016/j.jsse.2019.05.007.

[4] Mark F. Storz, Bruce R. Bowman, Major James I. Branson, Stephen J. Casali, and W. Kent Tobiska. High accuracy satellite drag model (HASDM). *Advances in Space Research*, 36(12):2497–2505, 2005. doi: 10.1016/j.asr.2004.02.020. Space Weather.

[5] Richard J. Licata. *Probabilistic Space Weather Modeling and Forecasting for the Challenge of Orbital Drag in Space Operations*. Doctoral dissertation, West Virginia University, Benjamin M. Statler College of Engineering and Mineral Resources, 2022.

[6] D.A. Vallado and W.D. McClain. *Fundamentals of Astrodynamics and Applications*. Microcosm Press, 2013.

[7] Ch. Reigber, H. Lühr, and P. Schwintzer. CHAMP mission status. *Advances in Space Research*, 30(2):129–134, 2002. doi: 10.1016/S0273-1177(02)00276-4.

[8] Byron D. Tapley, Srinivas Bettadpur, John C. Ries, Paul F. Thompson, and Michael M. Watkins. GRACE measurements of mass variability in the Earth system. *Science*, 305(5683):503–505, 2004. doi: 10.1126/science.1099192.

[9] Richard P. Kornfeld, Bradford W. Arnold, Michael A. Gross, Neil T. Dahya, William M. Klipstein, Peter F. Gath, and Srinivas Bettadpur. GRACE-FO: the gravity recovery and climate experiment follow-on mission. *Journal of Spacecraft and Rockets*, 56(3):931–951, 2019. doi: 10.2514/1.A34326.

[10] M. R. Drinkwater, R. Floberghagen, R. Haagmans, D. Muzi, and A. Popescu. VII: Closing session: GOCE: ESA's first Earth explorer core mission. *Space Science Reviews*, 108(1):419–432, Jul 2003. doi: 10.1023/A:1026104216284.

[11] E. Friis-Christensen, H. Lühr, and G. Hulot. Swarm: A constellation to study the Earth's magnetic field. *Earth, Planets and Space*, 58(4):351–358, Apr 2006. doi: 10.1186/BF03351933.

[12] J.T. Emmert, H.P. Warren, A.M. Segerman, J.M. Byers, and J.M. Picone. Propagation of atmospheric density errors to satellite orbits. *Advances in Space Research*, 59(1):147–165, 2017. doi: https://doi.org/10.1016/j.asr.2016.07.036.

[13] A. B. Poore, J. M. Aristoff, J. T. Horwood, and et al. Covariance and uncertainty realism in space surveillance and tracking. *Technical Report Defense Technical Information Center*, (AD1020892), June 2016.

[14] J. L. Foster and H. S. Estes. A parametric analysis of orbital debris collision probability and maneuver rate for space vehicles. *NASA/JSC-25898*, August 1992.

[15] Richard J. Licata and Piyush M. Mehta. Uncertainty quantification techniques for data-driven space weather modeling: thermospheric density application. *Scientific Reports*, 12(1):7256, May 2022. doi: 10.1038/s41598-022-11049-3.

[16] Richard J. Licata, Piyush M. Mehta, Daniel R. Weimer, W. Kent Tobiska, and Jean Yoshii. MSIS-UQ: Calibrated and Enhanced NRLMSIS 2.0 Model with uncertainty quantification. *Space Weather*, 20(11):e2022SW003267, 2022. doi: 10.1029/2022SW003267.

[17] Bruce Bowman, W. Kent Tobiska, Frank Marcos, Cheryl Huang, Chin Lin, and William Burke. A new empirical thermospheric density model JB2008 using new solar and geomagnetic indices. *AIAA/AAS Astrodynamics Specialist Conference and Exhibit*. doi: 10.2514/6.2008-6438.

[18] W. Kent Tobiska, Bruce R. Bowman, S. David Bouwer, Alfredo Cruz, Kaiya Wahl, Marcin D. Pilinski, Piyush M. Mehta, and Richard J. Licata. The SET HASDM density database. *Space Weather*, 19(4):e2020SW002682, 2021. doi: 10.1029/2020SW002682.

[19] J. T. Emmert, D. P. Drob, J. M. Picone, D. E. Siskind, M. Jones Jr., M. G. Mlynczak, P. F. Bernath, X. Chu, E. Doornbos, B. Funke, L. P. Goncharenko, M. E. Hervig, M. J. Schwartz, P. E. Sheese, F. Vargas, B. P. Williams, and T. Yuan. NRLMSIS 2.0: a whole-atmosphere empirical model of temperature and neutral species densities. *Earth and Space Science*, 8(3):e2020EA001321, 2021. doi: 10.1029/2020EA001321.

[20] D. R. Weimer, E. K. Sutton, M. G. Mlynczak, and L. A. Hunt. Intercalibration of neutral density measurements for mapping the thermosphere. *Journal of Geophysical Research: Space Physics*, 121(6):5975–5990, 2016. doi: 10.1002/2016JA022691.

[21] D. R. Weimer, P. M. Mehta, W. K. Tobiska, E. Doornbos, M. G. Mlynczak, D. P. Drob, and J. T. Emmert. Improving neutral density predictions using exospheric temperatures calculated on a geodesic, polyhedral grid. *Space Weather*, 18(1):e2019SW002355, 2020. doi: 10.1029/2019SW002355.

[22] Daniel R. Weimer, W. Kent Tobiska, Piyush M. Mehta, R. J. Licata, Douglas P. Drob, and Jean Yoshii. Comparison of a neutral density model with the SET HASDM density database. *Space Weather*, 19(12):e2021SW002888, 2021. doi: 10.1029/2021SW002888.

[23] Smriti Nandan Paul, Richard J. Licata, and Piyush M. Mehta. Advanced ensemble modeling method for space object state prediction accounting for uncertainty in atmospheric density. *Advances in Space Research*, 71(6): 2535–2549, 2023. doi: 10.1016/j.asr.2022.12.056.

[24] Bob Schutz, Byron Tapley, and George Born. *Statistical Orbit Determination*. Elsevier Academic Press, 2004.

[25] National Aeronautics and Space Administration. NASA spacecraft conjunction assessment and collision avoidance best practices handbook. Technical Report NASA/SP-20205011318, December 2020.

[26] M.D. Hejduk, D.E. Snow, and L.K Newman. Satellite conjunction assessment risk analysis for "dilution region" events: Issues and operational approaches. In *Space Traffic Management Conference*, 2019.

[27] Doyle T. Hall, Stephen J. Casali, Lauren C. Johnson, Brent B. Skrehart, and Luis G. Baars. High fidelity collision probabilities estimated using Brute Force Monte Carlo simulations. In *AAS/AIAA Astrodynamics Specialist Conference*, 2018.

[28] Maruthi R. Akella and Kyle T. Alfriend. Probability of collision between space objects. *Journal of Guidance, Control, and Dynamics*, 23(5):769–772, 2000. doi: 10.2514/2.4611.

[29] Salvatore Alfano and Daniel Oltrogge. Probability of collision: valuation, variability, visualization, and validity. *Acta Astronautica*, 148:301–316, 2018. doi: 10.1016/j.actaastro.2018.04.023.

[30] NASA. CARA Analysis Tools. `https://github.com/nasa/CARA_Analysis_Tools`, Accessed 2023.

[31] S.K. Pandey and S.C. Dubey. Characteristic features of large geomagnetic storms observed during solar cycle 23. *Indian Journal of Radio and Space Physics*, 38:305–312, 2009. URL `http://nopr.niscpr.res.in/handle/123456789/6897`.

[32] J.R. Dormand and P.J. Prince. A family of embedded Runge-Kutta formulae. *Journal of Computational and Applied Mathematics*, 6(1):19–26, 1980. doi: 10.1016/0771-050X(80)90013-3.

[33] R.B. D'Agostino. An omnibus test of normality for moderate and large size samples. *Biometrika*, 58(2):341–348, 08 1971. doi: 10.1093/biomet/58.2.341.

[34] R. D'Agostino and E.S. Pearson. Tests for departure from normality. Empirical results for the distributions of b_2 and $\sqrt{b_1}$. *Biometrika*, 60(3):613–622, 12 1973. doi: 10.1093/biomet/60.3.613.

[35] Pauli Virtanen, Ralf Gommers, Travis E. Oliphant, and et al. SciPy 1.0: Fundamental Algorithms for Scientific Computing in Python. *Nature Methods*, 17:261–272, 2020. doi: 10.1038/s41592-019-0686-2.